Technical University of Denmark

DTU

Numerical Simulations of Wakes of Wind Turbines Operating in Sheared and Turbulent Inflow

Troldborg, Niels; Sørensen, Jens Nørkær; Mikkelsen, Robert Flemming

Document Version
Publisher's PDF, also known as Version of record

[Link back to DTU Orbit](#)

DTU Library
Technical Information Center of Denmark

Numerical Simulations of Wakes of Wind Turbines Operating in Sheared and Turbulent Inflow

Niels Troldborg*, Jens N. Sørensen[†], Robert Mikkelsen[†]

*Wind Energy Department, Risø National Laboratory, DK-4000 Roskilde, Denmark
[†]Department of Mechanical Engineering, Fluid Mechanics Section, Technical University of Denmark, DK-2800 Kgs. Lyngby, Denmark

niels.troldborg@risoe.dk

Abstract

The wake of a wind turbine operating in a sheared and turbulent inflow at various inflow velocities is simulated using a numerical method, which combines large eddy simulations with an actuator line technique. The computations are carried out in a numerical mesh with about $8.4 \cdot 10^6$ grid points distributed to facilitate detailed studies of both the near and far wake. From the simulations basic properties of the wake is extracted with the objective of documenting the wake development in a standard shear and to study the influence of different assigned inflow turbulence fields on the stability of the wake vortex system.

1   Introduction

The motivation for studying wind turbine wakes is mainly that turbines grouped in wind farms operate partly or fully in the wake of other turbines hence experiencing a significantly modified wind field compared to an isolated turbine, which in effect causes reduced power production and increased fatigue loads.

The usual modelling approach used by industry for compensating for wake interaction is by increasing the overall turbulence level and decreasing the inflow velocity in the design process, however, with the disadvantages of not capturing the actual turbulence characteristics properly. Nor does such a modelling approach satisfactorily accounts for the mechanism of wake deficit meandering, which has been observed in field measurements and may contribute significantly to the increased loads of downstream turbines.

The influence of shear further complicates the description of wakes since the assumption of axisymmetry and self-similarity usually adopted in far wake models no longer is valid. Both numerical [24], [21] and experimental [5], [22] investigations have shown that the dynamics of wakes in shear flow may be considerably more complex than in free shear flows.

Despite extensive research in wind turbine wakes [23] there is still a need in the wind turbine industry for a reliable engineering model for describing the load conditions of wind turbines in wind farms. Recently, however, Larsen and colleges [6], [7] presented a consistent physical theory for describing the dynamic wake meandering. The basic conjecture behind the so-called Dynamic Wake Meandering Model (DWM) is that wake meandering is governed by the large scale lateral and vertical turbulence components in the atmosphere - an interpretation which has been supported both by full scale measurements [1] and in numerical simulations [21]. To complete the theory of the DWM model, the formulation of the meandering was further combined with sub models for respectively the velocity deficit and the added wake turbulence in the meandering frame of reference. In developing these sub models detailed knowledge is required not only about the mean properties of the meandering wake but also about its turbulence characteristics. Such detail are rarely provided to a satisfactory degree from field measurements due to limited data acquisition and/or insufficient knowledge about the ever changing inflow. Therefore, it is advantageous to use numerical methods because the inflow conditions then are easily controlled and since all relevant flow properties are described in detail.

This paper presents 3D Navier Stokes simulations of the wake of a wind turbine operating in sheared and turbulent inflow using the actuator line technique combined with Large Eddy Simulations. The computations are carried out in a numerical mesh with a high concentration of grid points distributed to facilitate detailed studies of both the near and far wake. Simulations are carried out on a wind turbine operating at inflow velocities at hub height of $V_\infty = 5\,m/s$, $10\,m/s$ and $15\,m/s$, which represent four very different operational conditions of the turbine. The objective of the paper is to extract general features of wind turbine wakes and to study how the stability properties of the wake vortex system are affected by the presence of shear and different degrees of ambient turbulence.

2   Numerical Modelling

In this section the models used for simulating the turbine and the atmospheric boundary layer is presented.

2.1   The Actuator Line Method

The wind turbine rotor was simulated using the actuator line model developed by Sørensen and Shen [17]. This model combines a three-dimensional Navier-Stokes solver with a technique in which body forces are distributed radially along lines representing the blades of the wind turbine. Thus, the flow field around and downstream of the rotor is governed by full three-dimensional Navier-Stokes simulations, whereas the influence of the rotating blades on the flow field is computed by calculating the local angle of attack and then determining the local forces from tabulated airfoil data. Originally the method was formulated in vorticity-velocity variables but later Mikkelsen [12] reformulated it in primitive variables (pressure-velocity) in order to combine it with the flow solver $EllipSys3D$ to be described later.

The advantage of representing the blades by airfoil data, as it is done in the actuator line model, is that much fewer grid points are needed to capture the influence of the blades compared to what would be needed for simulating the actual geometry of the blades.

2.2   Flow solver - EllipSys3D

The computations of the global flow field have been carried out using the 3D flow solver $EllipSys3D$ developed by Michelsen [10], [11] and Sørensen [18]. This code solves the discretized incompressible Navier-Stokes equations in general curvilinear coordinates using a block structured finite volume approach. EllipSys3D is formulated in primitive variables (pressure-velocity) in a non-staggered grid arrangement. The pressure correction equation was solved using the SIMPLE algorithm and pressure decoupling is avoided using the Rhie/Chow interpolation technique. The convective terms were discretized using a hybrid scheme combining the third order accurate QUICK (10%) scheme and the fourth order CDS scheme (90%). Large eddy simulation (LES) was used to model the small length scales of turbulence. The resulting equations thus only govern the dynamics of the large scales, while the small scales here were modelled using the so-called mixed scale model [15], [16].

2.3   Modelling the atmospheric boundary layer

The atmospheric boundary layer is modelled using a technique where body forces applied to the entire computational domain is used to impose a given but arbitrary steady wind shear profile, while free-stream turbulence is modelled by introducing synthetic turbulent velocity fluctuations to the mean flow upstream of the rotor.

2.3.1   Modelling the mean wind shear

The method of imposing a given wind shear profile by applying body forces was presented by Mikkelsen et al. [13] and described in more detail by Troldborg [21]. The idea is to conduct an initial computation without the wind turbine included in the domain in order to establish the force field required to obtain a desired prescribed mean wind shear profile. The obtained steady force field is afterwards stored and fixed in the subsequent computation where the wind turbine is included.

In all of the computations presented in this work the velocity profile is prescribed to follow a power law profile.

$$V_0 = V_\infty \left(\frac{y}{H} \right)^\alpha \tag{1}$$

where H is the hub height of the wind turbine, V_∞ is the mean wind speed at hub height and y is the height above ground.

2.3.2   Modelling the atmospheric turbulence

The atmospheric inflow turbulence was simulated using a technique [20] where unsteady concentrated body forces, introduced in a $5R \times 5R$ plane located $1R$ upstream of the rotor, are producing the synthetic turbulent velocity fluctuations. The introduced turbulence field was generated in advance by using the Mann algorithm [8], [9], which simulates homogenous, stationary, Gaussian and anisotropic turbulence with the same spectral characteristics as observed in the atmosphere.

2.4   Computational domain & boundary conditions

The computations have been conducted in a Cartesian computational domain with dimensions $(L_x, L_y, L_z) = (24R, 20R, 26.8R)$, where L_z denotes the domain length (in the flow direction), L_y the domain height, L_x the domain width and R is the rotor

radius.

The actuator lines were in all cases positioned $7R$ downstream of the inlet and the center of rotation was located midway between the two lateral boundaries at a height according to the hub height of the given turbine.

A high concentration of grid points was distributed equidistantly in the region around and downstream of the rotor in order to resolve and preserve the generated flow structures in the wake. The dimensions of the equidistant region, occasionally referred to as the near domain, were $2.6R \times 2.6R$. Outside the equidistant region grid points were stretched away toward the outer boundaries. The resolution in the near domain corresponded to 30 grid points per rotor radius. The grid consisted of 128 grid points in respectively the x and y direction and 512 grid points in z-direction.

The boundary conditions were as follows: The velocity was specified according to the wanted shear profile at the inlet, unsteady convective conditions at the outlet, no-slip at the ground, far-field velocity at the top boundary and periodic conditions on the sides.

A similar grid configuration was used in [21] and was through a mesh study shown to be sufficient to resolve the most important features of the wake.

2.5 Wind Turbine

The computations were conducted using airfoil data from the 3MW NM80 wind turbine. The blade radius of this turbine is $R = 40.04\,m$ and it has a variable rotational speed depending on the wind speed; at $V_\infty = 5\,m/s$ the rotational speed is $\Omega = 11.2\,RPM$, and at $V_\infty = 20\,m/s$ it is $\Omega = 17.2\,RPM$. Further technical details about the NM80 turbine can be found in [4].

3 Results

In the following some results from the simulations of the wake of the NM80 turbine are presented. Computations were carried out at inflow velocities at hub height of $V_\infty = 5\,m/s$, $10\,m/s$ and $15\,m/s$ and a shear coefficient of $\alpha = 0.2$. For each case three different inflow conditions are imposed: one at laminar conditions ($\sigma_\infty = 0$), one where the generated ambient turbulence is isotropic with an intensity of $\sigma_\infty/V_\infty = 0.01$ and one where the ambient turbulence is generated according to the Kaimal spectrum and has a turbulence intensity of $\sigma_\infty/V_\infty = 0.09$.

3.1 Validation

In order to verify that the used blade and airfoil data are suitable for simulating the NM80 rotor the power coefficient was computed and compared to experiments in figure 1. Generally, the agreement is good, which suggests that the used blade data is proper. The reason that the computed power is higher than the measured is that the computed curve represents mechanical power whereas the measured is electrical.
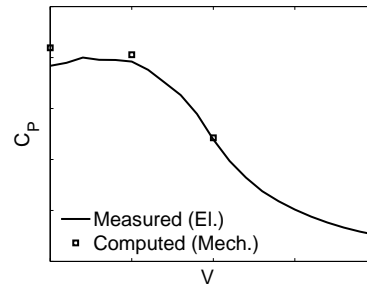

Figure 1: *Power coefficient as a function of inflow velocity*

To further validate the simulations, figure 2 and 3 compares the computed and measured profiles of respectively the mean streamwise velocity and turbulence intensity at hub height in a section located $2.5D$ downstream of the turbine operating at $V_\infty = 10\,m/s$ and $\sigma_\infty/V_\infty = 0.09$.
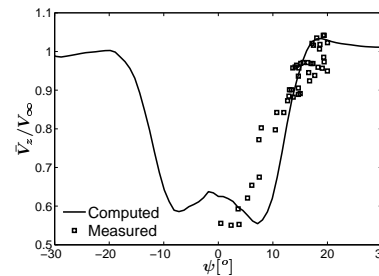

Figure 2: *Computed and measured profiles of the time averaged streamwise velocity plotted against wind direction $2.5D$ downstream of the rotor. $V_\infty = 10\,m/s$ and $\sigma_\infty/V_\infty = 0.09$*

Note that for the measured mean velocity data, ambient wind speeds in the range $9 - 11\,m/s$ have been considered, reflecting the usual balance, between amount of available data and the selected bin size [6]. The simulated results of both mean velocity and standard deviation agree reasonable with the measured data, though it seems that the predicted turbulence level is somewhat too low. However, the limited amount of measured data and the rather significant

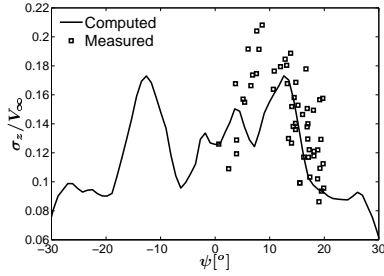scatter makes the comparison somewhat inconclusive in terms of wake shape.

Figure 3: *Computed and measured profiles of the streamwise turbulence intensity plotted against wind direction* $2.5D$ *downstream of the rotor.* $V_\infty = 10m/s$ *and* $\sigma_\infty/V_\infty = 0.09$

3.2 Wake characteristics

Figures 4-5, for different inflow turbulence levels, show representative contours of the instantaneous absolute vorticity in a vertical plane intersecting the rotor center axis at respectively $V_\infty = 5m/s$ and $15m/s$. Regions of high vorticity appear as light colors and the rotor is located to the left in the plots. The corresponding plots at $V_\infty = 10\,m/s$ are not shown here since they reveal a wake behavior in between the two other cases.
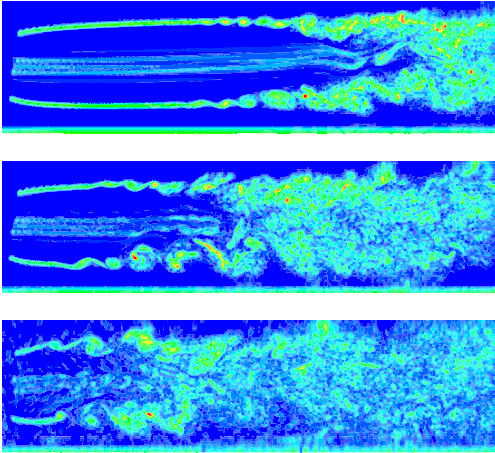

Figure 4: *Downstream development of the wake of the turbine operating at* $V_\infty = 5\ m/s$ *visualized using vorticity contours. The rotor is located to the left; From top to bottom:* $\sigma_\infty/V_\infty = 0$, 0.01 *and* 0.09

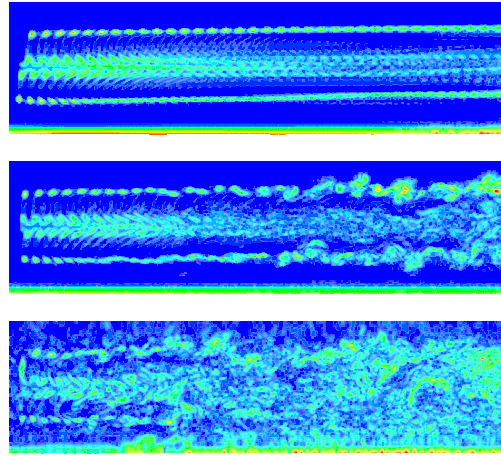In both cases the bound vorticity of the blades is primarily shed downstream from the tip and root of

Figure 5: *Downstream development of the wake of the turbine operating at* $V_\infty = 15\ m/s$ *visualized using vorticity contours. The rotor is located to the left; From top to bottom:* $\sigma_\infty/V_\infty = 0$, 0.01 *and* 0.09

the rotor. At $V_\infty = 15\ m/s$ the individual tip vortex tubes are resolved several rotor diameters downstream, whereas they at $V_\infty = 5\ m/s$ smear into a continuous vorticity sheet immediately downstream of the rotor due to the limited grid resolution and low pitch of the vortex system. As expected, a consequence of the inflow velocity shear is that the transport of the tip vortices is larger when in the top position than when in the bottom position.

From the figures it is evident that even low levels of ambient turbulence causes dramatic changes in the wake development. In laminar inflow the wake of the rotor operating at $V_\infty = 15\ m/s$ remains stable throughout the entire investigated area, while it breaks up some distance downstream at $V_\infty = 5\ m/s$ due to the larger C_T of the rotor in this case.

When the isotropic low turbulent field is imposed the vortex system is continuously perturbed whereby the wake becomes unstable much closer to the rotor than when the inflow is laminar. However, at $V_\infty = 15\ m/s$ the tip and root vortices are more persistent and stay separated from each other within the studied region. Therefore, the wake does not break up completely into small scale turbulence in this case.

When the 9% turbulence field is imposed the wake in both cases appears to become fully turbulent only few diameters downstream.

Figure 6-7 show contours of the mean streamwise induction $\Delta \bar{V}_z = V_0 - \bar{V}_z$ at different positions downstream of the rotor operating in a 9% turbulence field at respectively $V_\infty = 5\ m/s$ and $15\ m/s$. The view is from downwind, i.e. the azimuth position corresponding to 0° is to the right and the wake
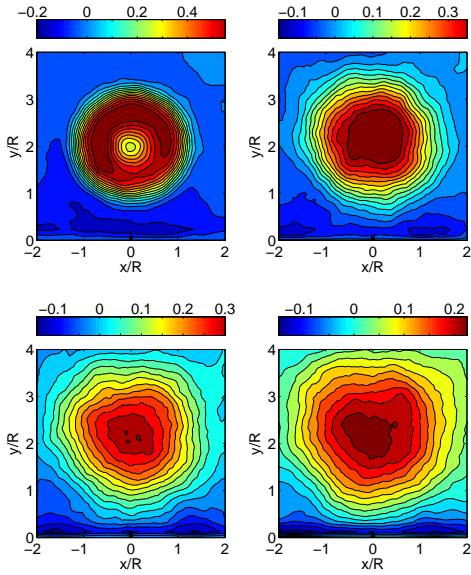
rotates clockwise.

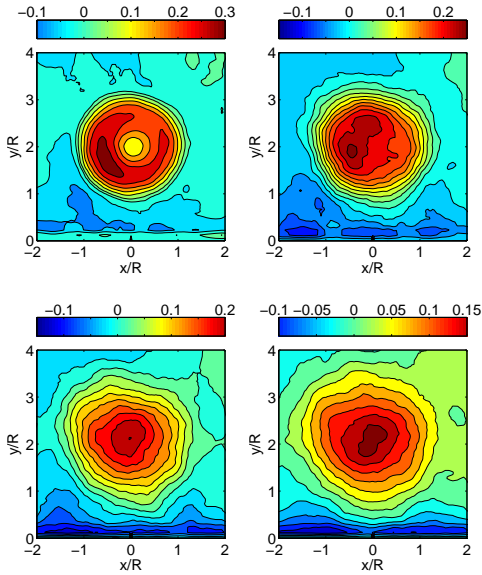Figure 6: *Mean induction contours at $V_\infty = 5\,m/s$. From left to right: 3R, 7R, 11R and 15R downstream*

Figure 7: *Mean induction contours at $V_\infty = 15\,m/s$. From left to right: 3R, 7R, 11R and 15R downstream*

In agreement with previous observations [24], [21] the rotation of the wake creates a horizontal asymmetry in the velocity deficit. However, as the wake breaks up into small scale turbulence, the mean swirl goes toward zero and thus the horizontal asymmetry gradually diminishes. It should be noted that at lower ambient turbulence levels the asymmetric

redistribution of the velocity deficit remains clear much further downstream than in the two shown cases. In both cases it is clear that the presence of the ground causes the wake to expand more upwards and to the sides than downwards. Furthermore, the ground results in a speed up under the wake region.
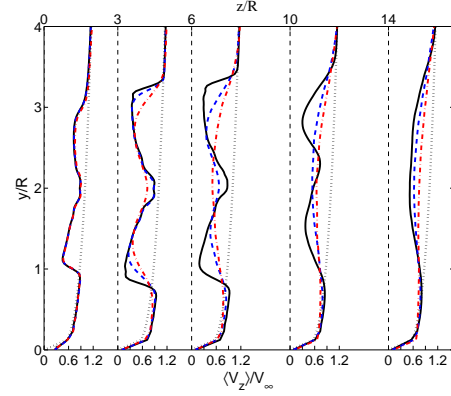

Figure 8: *Mean streamwise velocity profiles in the vertical plane through the rotor center at $V_\infty = 5\,m/s$. The downstream location is indicated in the top axis. Full line: $\sigma_\infty/V_\infty = 0$; Dashed line: $\sigma_\infty/V_\infty = 0.01$; Dash-dot line: $\sigma_\infty/V_\infty = 0.1$*

Figure 9: *Mean streamwise velocity profiles in the vertical plane through the rotor center at $V_\infty = 15\,m/s$. The downstream location is indicated in the top axis. Full line: $\sigma_\infty/V_\infty = 0$; Dashed line: $\sigma_\infty/V_\infty = 0.01$; Dash-dot line: $\sigma_\infty/V_\infty = 0.1$*
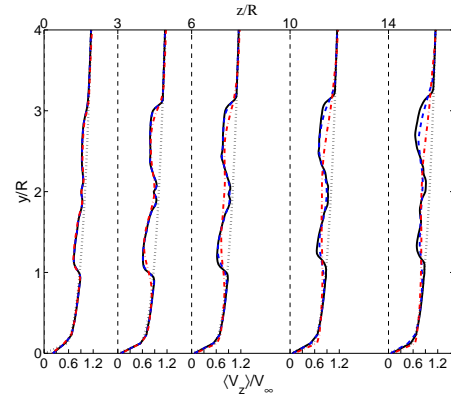
Figure 8-9 show the downstream development of the time averaged streamwise velocity in a vertical plane going through the rotor center axis at respectively $V_\infty = 5\,m/s$ and $V_\infty = 15\,m/s$. In order to give an impression of the induction the inlet velocity profile (equation 1) is also included in the figures.

The ambient turbulence field causes the wake to

undergo a more rapid transition into a bell shaped form than when the inflow is laminar as expected. Furthermore, it appears that the maximum deficit is located slightly above the wind turbine center axes. This observation is most probably due to the presence of the wall but could also be a reminiscent from the near wake, where the induction is largest in the upper part of the wake.

The downstream development of the center line velocity deficit has been evaluated for selected cases and the result is presented in $\log-\log$ plots in Figure 10-11. The different cases are identified in the legend by the rotor thrust coefficient: The thrust coefficient of the NM80 turbine is $C_T = 0.87, 0.71$ and 0.43 for inflow velocities of respectively $V_\infty = 5\,m/s, 10\,m/s$ and $15m/s$. Also shown in the figures are results from actuator line computations conducted on other turbines as well as their comparison with measurements. Initially, it is noted that the agreement between measured and computed center line velocity deficit generally is good. A more thorough comparison of computations and measurements has been conducted and will be presented in later work.
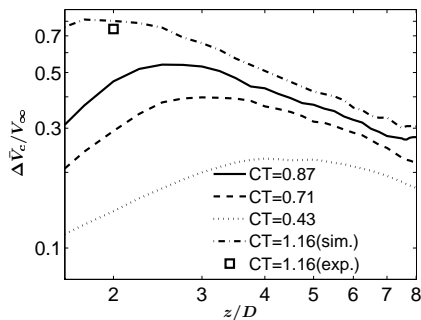

Figure 10: *Center line velocity deficit as a function of downstream distance; C_T varied while $\sigma_\infty = 9\%$. Measurements at $C_T = 1.16$ from [3]*

In Figure 10 the ambient turbulence level is approximately 9%, while the curves represent different C_T levels. As expected the location where wake recovery initiates moves upstream with increasing thrust level. In the far wake all curves seem to be nearly linear with approximately the same slope, which is in agreement with theoretical expectations [14]. A least square fit has been conducted on the linear part of each curve and the slope was found to be in the range -0.75 to -0.85.

Figure 11 shows the corresponding development where the thrust level is approximately constant ($C_T = 0.84 - 0.91$), while the ambient turbulence level is varied between 1% and 12%. The downstream
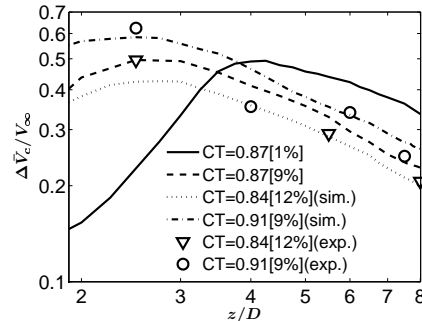

Figure 11: *Center line velocity deficit as a function of downstream distance; σ_∞ varied while C_T is nearly constant. Measurements at $C_T = 0.9$ and 0.84 from [19] and [2], respectively.*

position where the wake deficit begins to recover generally moves upwind with increasing turbulence level, as expected. However, it appears that the position of recovery at respectively 9% and 12% does not differ significantly. The reason for this could be due to differences in rotor properties and that C_T in the 12% ambient turbulence case is slightly lower than in the other cases. Once again the curves in the far wake are nearly linear but in the 1% ambient inflow turbulence case the slope is clearly lower than in the other cases, as expected. A least square fit revealed a slope of approximately -0.7 in the former case and -0.85 in the latter cases. The value of -0.7 is in good agreement with theoretical expectations for axis-symmetric far wakes in non-turbulent inflow [14].

Figure 12 and 13 show the corresponding behavior of the maximum added turbulence at hub height. The added turbulence is here computed as

$$\Delta\sigma_z = \sqrt{\sigma_z^2 - \sigma_\infty^2} \qquad (2)$$

Where σ_z is the standard deviation in the wake and σ_∞ is the standard deviation of the ambient turbulence field. Once again, the comparison of measured and computed values reveal quite good agreement.

From figure 12 it is evident that the added turbulence level generally increase with increasing C_T, as expected. Similar to what was observed for the centerline wake deficit the curves of the added turbulence appear somewhat linear in the far wake. However, the trend is not as clear in the present case due to limited statistical data.

Figure 13 shows the development of the maximum added turbulence for different ambient turbulence levels. In the far wake all curves appear approximately linear but with slightly different slopes. A least square fit showed that $\Delta\sigma$ decays approximately
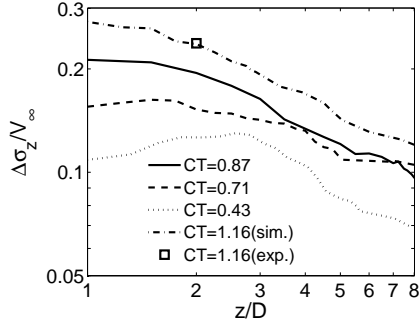
Figure 12: *Maximum added turbulence intensity at hub height as a function of downstream distance; C_T varied while $\sigma_\infty = 9\%$. Measurements at $C_T = 1.16$ from [3]*

with a slope of -0.7 in the wake when $\sigma_\infty/V_\infty = 0.01$, while the slope only is about -0.55 in the other cases. Furthermore, it is clear that the added turbulence in the wake of the rotor operating in the 1% ambient turbulence field is shifted upwards and right compared to the other cases. This behavior is caused by a delayed downstream breakdown of the vortex system when the ambient turbulence is low.
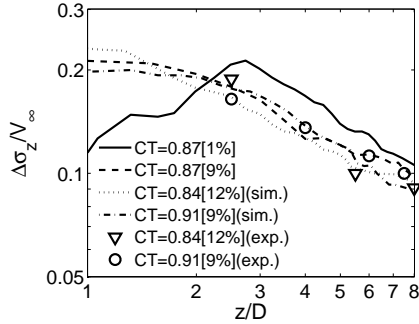

Figure 13: *Maximum added turbulence intensity at hub height as a function of downstream distance; σ_∞ varied while C_T is nearly constant. Measurements at $C_T = 0.9$ and 0.84 from [19] and [2], respectively.*

Similar to the usual practice for axisymmetric turbulent far wakes [14] a characteristic half wake width $r_{1/2}$ is in the following defined from:

$$V_0(r,\theta) - \langle V_z(r_{1/2}, \theta, z)\rangle = \frac{1}{2}\Delta V_z \qquad (3)$$

where V_0 is the inflow velocity given by equation 1 expressed in polar coordinates and $\Delta \bar{V}_c$ is the centerline velocity deficit. Due to the inflow shear, the wake is not axisymmetric and hence $r_{1/2}$ depends both on downstream position and azimuth angle.
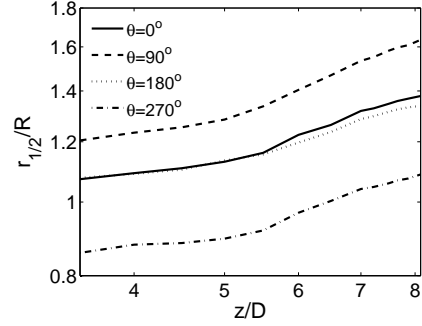

Figure 14: *Half wake width as a function of downstream position at different azimuth angles. $V_\infty = 5\,m/s$ and $\sigma_\infty/V_\infty = 0.09$*

Figure 14 show the variation of $r_{1/2}$ as a function of downstream position for four distinct azimuth angles in the wake of the rotor operating at $V_\infty = 5\,m/s$ and $\sigma_\infty/V_\infty = 9\%$. Consistent with the observations made from the contours of induction in figure 6 the wake expands more upwards and to the sides than downwards. Still, however, the overall trend followed by the curves is more or less the same. In the far wake a least square fit showed that $r_{1/2}$ varied approximately as $z^{0.45}$ in the upward direction and as $z^{0.4}$ in the other directions.
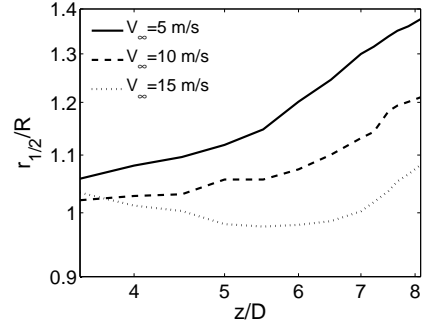

Figure 15: *Half wake width as a function of downstream position for different V_∞; $\sigma_\infty/V_\infty = 0.09$*

Figure 15 show the downstream development of the circumferentially averaged $r_{1/2}$ at $\sigma_\infty/V_\infty = 9\%$ and inflow velocities of $V_\infty = 5\,m/s$, $10\,m/s$ and $15\,m/s$. For the two highest inflow velocities the trend followed is similar to that shown in figure 14. At $V_\infty = 15\,m/s$ on the other hand $r_{1/2}$ initially decrease slightly before it approximately 6D downstream begins to increase. The initial decrease of $r_{1/2}$ does not reflect an actual wake contraction but is merely a consequence of the wake not being fully developed, cf. figure 9.

In order to study the large scale dynamics of the wake the temporal evolution of the wake center was computed. Inspired by the work of Trujillo et al. [22], a wake center is here determined by fitting a 2D Gaussian surface to the unsteady wake deficit using a least square approach. That is, for a given downstream position, each of a series of instantaneous snapshots of the induction are fitted with the following expression

$$f = \frac{A}{2\pi\sigma_x\sigma_y}\exp\left(-\frac{(x-\mu_x)^2}{2\sigma_x^2} - \frac{(y-\mu_y)^2}{2\sigma_y^2}\right) \quad (4)$$

where, μ_x and μ_y are respectively the x and y coordinates of the wake center.

Figure 16 shows the standard deviation of the wake center coordinates as a function of downstream position for three selected cases. The standard deviation of the x-coordinate σ_{cx} increase nearly linearly with downstream position with the steepest slope, as expected, obtained at the highest ambient turbulence levels. The linear increase is consistent with the passive tracer analogy of wakes assumed in the DWM model [7]. The reason that σ_{cy} does not increase linearly is most likely due to the presence of the ground.
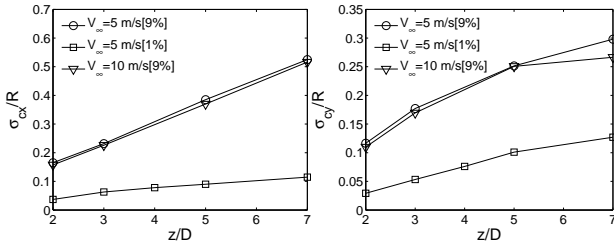
Figure 16: *Standard deviation of wake center fluctuations in respectively the x and y direction.*

The streamwise induced velocity profile ensemble averaged around the dynamic wake center has been computed for different downstream sections and compared with the corresponding profile in the fixed frame of reference. As a representative example figure 17 shows the results obtained at four distinct azimuth angles 7D downstream of the rotor operating at $V_\infty = 5\,m/s$ and $\sigma_\infty/V_\infty = 9\%$. As expected, the velocity deficit computed in the meandering frame of reference is clearly characterized by being deeper and having a smaller radial extent than the deficit computed in the fixed frame. Another interesting observation is that the wake in the meandering frame of reference only is vaguely sensitive to changes in azimuth position, i.e. the meandering wake on average appears rather circular.

Since the far wake velocity deficit expressed in the meandering frame of reference cf. figure 17 is rota-
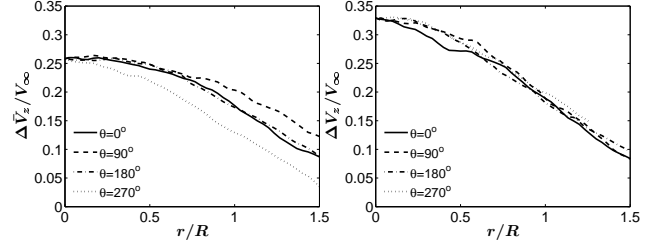
Figure 17: *Averaged streamwise velocity 7D downstream of the rotor computed in respectively a fixed (left) and a meandering (right) frame of reference.* $V_\infty = 5\,m/s$, $\sigma_\infty/V_\infty = 0.09$

tionally symmetric and Gaussian it can be approximated as

$$\Delta V_z(x,y) = \Delta V_c \exp(-\frac{r^2}{2\sigma_r^2}) \quad (5)$$

where $r^2 = x^2 + y^2$ and σ_r is the standard deviation of the velocity distribution.

The mean velocity deficit in the meandering frame of reference is linked to the deficit in the fixed frame through a convolution integral

$$\Delta \bar{V}_z = \Delta V_z \otimes G \quad (6)$$

where G is the probability density function of the wake center fluctuations.

The distribution of the wake center fluctuations was found to be rather Gaussian, which is as expected since the ambient turbulence field is also Gaussian distributed. Thus the distribution of the wake center fluctuations may be expressed as

$$G(x,y) = \frac{\int_{-\infty}^{\infty} \exp(-\frac{(x-\mu_x)^2}{2\sigma_{cx}^2} - \frac{(y-\mu_y)^2}{2\sigma_{cy}^2})dxdy}{2\pi\sigma_{cx}\sigma_{cy}} \quad (7)$$

where σ_{cx} and σ_{cy} is the standard deviation of the wake center fluctuations in respectively the x and y direction.

Inserting 5 and 7 into equation 6 and integrating gives:

$$\Delta \bar{V}_z = \Delta V_c \frac{\sigma_r^2 \exp(-\frac{(x-\mu_x)^2}{2(\sigma_r^2+\sigma_{cx}^2)} - \frac{(y-\mu_y)^2}{2(\sigma_r^2+\sigma_{cy}^2)})}{\sqrt{(\sigma_r^2+\sigma_{cx}^2)(\sigma_r^2+\sigma_{cy}^2)}} \quad (8)$$

In figure 18 the results of equation 8 is compared with the actual induction shown in the left plot of figure 17 for four distinct azimuth angles. The values of ΔV_c and σ_r was determined from a least square fit of equation 5 to the average of the curves in the right

plot of figure 17, while σ_{cx} and σ_{cy} was given from figure 16. As seen the agreement is fair for the horizontal and downward directions, whereas equation 8 over predicts the induction in the upward direction. The differences is mainly due to all the other dynamics taking place in the wake.
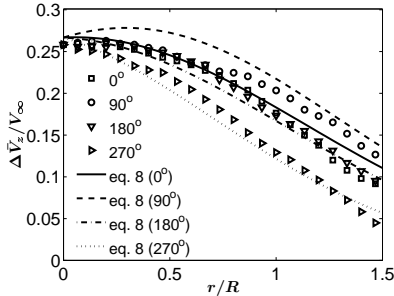

Figure 18: *Comparison of mean streamwise velocity 7D downstream of the rotor with predictions of equation 8. $V_\infty = 5\,m/s$, $\sigma_\infty/V_\infty = 0.09$*

As a final investigation the turbulence properties 7D downstream of the rotor operating at $V_\infty = 5\,m/s$ and $\sigma_\infty/V_\infty = 9\%$ was studied. The turbulent fluctuations in the streamwise direction is considered consisting of two parts:

$$v_z = v_m + v_w \qquad (9)$$

where v_m is the velocity fluctuations caused by the meandering of the wake and v_w is the turbulence in the meandering frame of reference. Figure 19 shows the standard deviation of v_z and v_w at the given downstream section for four distinct azimuth angles. As seen the turbulence expressed in the meandering
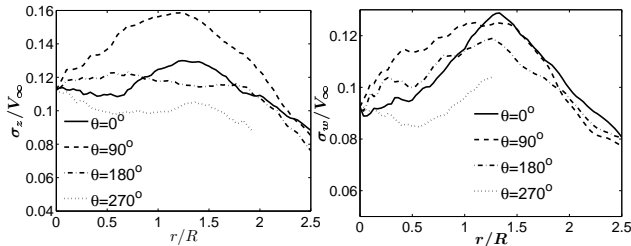

Figure 19: *Turbulence intensity profiles 7D downstream of the rotor computed in respectively a fixed (left) and a meandering (right) frame of reference.$V_\infty = 5\,m/s$, $\sigma_\infty/V_\infty = 0.09$*

frame of reference is generally lower and appears to be more rotationally symmetric than in the fixed frame. The standard deviation caused by the meandering of

the instantaneous wake can be estimated by solving the following convolution integral

$$\sigma_m^2 = (\Delta V_z - \Delta \bar{V}_z)^2 \otimes G \qquad (10)$$

where ΔV_z, $\Delta \bar{V}_z$ and G are given by equation 5, 6 and 7, respectively. Carrying out the integration yields

$$\sigma_m^2 = \Delta V_c^2 \frac{\sigma_r^2 \exp(-\frac{x^2}{\sigma_r^2 + 2\sigma_{cx}^2} - \frac{y^2}{\sigma_r^2 + 2\sigma_{cy}^2})}{\sqrt{(\sigma_r^2 + 2\sigma_{cx}^2)(\sigma_r^2 + 2\sigma_{cy}^2)}} - \Delta \bar{V}_z^2 \quad (11)$$

Figure 20 compares the different components of the turbulence field in the section located 7D downstream of the rotor at $V_\infty = 5\,m/s$ and $\sigma_\infty/V_\infty = 9\%$ for the horizontal direction $\theta = 0^o$. The figure clearly reveal
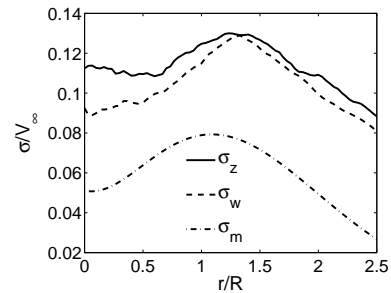

Figure 20: *The different components of the turbulence intensity profiles 7D downstream of the rotor in the horizontal direction $\theta = 0^o$. $V_\infty = 5\,m/s$, $\sigma_\infty/V_\infty = 0.09$*

that wake meandering contributes significantly to the total apparent turbulence in the wake.

4 Conclusion

The wake of a wind turbine subject to sheared and turbulent inflow conditions have been simulated using the Navier Stokes solver *EllipSys*3D and the actuator line technique combined with refined modelling of wind shear and elegant inclusion of ambient turbulence using the Mann turbulence generator. Computations were carried out at inflow velocities at hub height of $V_\infty = 5\,m/s$, $10\,m/s$ and $15\,m/s$ and a shear coefficient of $\alpha = 0.2$. For each case, three inflow conditions were imposed ranging from a laminar inflow to an inflow with a turbulence intensity of 9%.

The computations showed that even low levels of ambient turbulence causes dramatic changes in the wake development. The ambient turbulence perturbs the helical vortex system whereby the wake breaks up in a chaotic process resulting in increased turbulence levels inside the wake.

The inflow shear and presence of ground causes an asymmetric development of the wake with larger expansions upwards and to the sides than downwards.

Fundamental properties of the wake have been extracted including downstream development of wake center deficit, added wake turbulence and wake width. A comparison of deficit and added turbulence with field measurements showed good agreement.

The standard deviation of the meandering wake center was found to increase nearly linearly with downstream position. Another interesting finding was that the characteristics of the far wake described in the meandering frame of reference was much more axisymmetric than in a fixed frame.

References

[1] Bingöl, F. Mann, J. and Larsen, G.C. Lidar measurements of wake dynamics part 1: One dimensional scanning. Submitted to Wind Energy.

[2] Cleijne, J.W. Results of Sexbierum wind farm. Report 92-388, TNO-MT, Netherlands, 1992.

[3] Hansen, K.S. WP 4.2 Wake data analysis (working draft). EU-TOPFARM. 2009.

[4] Hansen, M.H., Fuglsang, P. and Thomsen K. Aeroelastic modeling of the NM80 turbine with HAWC. Risø-I-2017(EN). Risø National Laboratory, Technical University of Denmark, 2004.

[5] Högström, U., Asimakopoulost, N. Kambezidis, H., Helmis, C.G. and Smedman, A. A field study of the wake behind a 2 MW wind turbine. Atmopsheric Environment, Vol. 22, No. 4. 1988.

[6] Larsen, G.C. et al. Dynamic wake meandering modelling. Risø-R-1607(EN). Risø National Laboratory, Technical University of Denmark, 2007.

[7] Larsen, G.C., Madsen, H.Aa., Thomsen, K. and Larsen, T.J. Wake Meandering - A pragmatic Approach. Wind Energy, 2008.

[8] Mann, J. The spatial structure of neutral atmospheric surface-layer turbulence. Journal of Fluid Mechanics, 273, 141-168, 1994.

[9] Mann, J. Wind field simulation. Prob. Eng. Mech., Vol. 13, No. 4, 1998

[10] Michelsen, J.A. Basis3D - a Platform for Development of Multiblock PDE Solvers. Report AFM 92-05, Dept. of Fluid Mechanics, Technical University of Denmark, DTU, 1994.

[11] Michelsen, J.A., Block Structured Multigrid Solution of 2D and 3D elliptic PDE's, Report AFM 94-06, Dept. of Fluid Mechanics, Technical University of Denmark, DTU, 1994.

[12] Mikkelsen, R., Actuator Disc Methods Applied to Wind Turbines, MEK-FM-PHD 2003-02, Technical University of Denmark, 2003.

[13] Mikkelsen, R., Sørensen, J.N. and Troldborg, N. Prescribed Wind Shear Modelling Combined with the Actuator Line Technique. EWEC, Milan, 2007.

[14] Pope, S.B. Turbulent Flows. Cambridge University Press, 2000.

[15] Ta Phuoc, L., Lardat, R, Coutanceau, M. and Pineau, G. Rechereche et analyse de modeles de turbulence de sous maille adaptes aux ecoulments instationaires decolles. LIMSI Report 93074, LIMSI, France, 1994.

[16] Saugaut, P., Large Eddy Simulation for Incompressible Flows - An Introduction, Springer, 2005

[17] Sørensen, J.N. and Shen, W.Z. Numerical modelling of Wind Turbine Wakes. Fluids Engineering, Vol. 124, Issue 2, 2002.

[18] Sørensen, N.N., General Purpose Flow Solver Applied to Flow over Hills, PhD thesis, Risø-R-827(EN), Risø National Laboratory, 1995.

[19] Taylor, G.J. Wake measurements on the Nibe turbines in Denmark. ETSU WN 5020, 1990.

[20] Troldborg, N., Sørensen, J.N. and Mikkelsen, R. Actuator Line Simulation of Wake of Wind Turbine Operating in Turbulent Inflow. Journal of Physics: Conference Series. The Science of Making Torque from Wind. Technical University of Denmark, 2007.

[21] Troldborg, N., Actuator Line Modeling of Wind Turbine Wakes, PhD Dissertation, Technical University of Denmark, 2008.

[22] Trujillo, JJ, Bingöl, F., Larsen, G.C., Mann, J. and Kühn. lidar Measurements of Wake Dynamics Part II: two-dimensional scanning. Submitted to Wind Energy.

[23] Vermeer, L.J., Sørensen, J.N. and Crespo, A. Wind Turbine Wake Aerodynamics. Progress in Aerospace Sciences, Vol. 39, pp. 467-510, 2003.

[24] Zahle, F. and Sørensen, N.N. Rotor Aerodynamics in Shear Flow. EWEC, Bruxelles, 2008.